Maejo International Journal of
Energy and Environmental Communication
Journal home page: https://ph02.tci-thaijo.org/index.php/MIJEEC

RESEARCH ARTICLE

First-principles insights into the structural, mechanical, electronic, and optical properties of $LiRhH_3$ perovskite hydride: A comprehensive computational study for hydrogen storage applications

Tehreem Tariq[1,2,*]

[1]*Dipartimento di Fisica e Astronomia "Galileo Galilei", University of Padova, Padua, Italy*
[2]*INFN – Sezione di Padova, Padua, Italy*

ARTICLEINFO

Article history:

Received: 12 November 2025
Revised: 28 December 2025
Accepted: 19 January 2026
Published: 20 January 2026

Keywords:

$LiRhH_3$
Perovskite hydride
Density functional theory
Hydrogen storage
Elastic anisotropy
Optical properties

Abstract

Perovskite-type ABH_3 hydrides are attractive candidates for safe solid-state hydrogen storage, but the physical properties of many transition-metal compositions are still unknown. In this work, the structural, electronic, mechanical and optical properties of the rhodium-based perovskite hydride $LiRhH_3$ were investigated by density functional theory (DFT) with the GGA–PBE functional in CASTEP. The optimized structure is a tilt-free cubic perovskite, and the simulated X-ray diffraction pattern shows sharp (100), (110) and (111) reflections with no impurity or superstructure peaks. The elastic constants satisfy the Born stability criteria, and the bulk modulus of 91.015 GPa indicates strong resistance to volume change. Pugh's and Poisson's ratios indicate ductile, predominantly ionic behavior, while directional plots of Young's modulus, shear modulus and Poisson's ratio reveal moderate elastic anisotropy with almost isotropic linear compressibility. Bands cross the Fermi level with a low density of states, giving metallic character governed by Rh d–H 1s hybridization. $LiRhH_3$ absorbs strongly in the ultraviolet, with an absorption maximum near 291 nm and an energy-loss (plasma) peak at 23.76 eV. Its theoretical gravimetric hydrogen capacity is 2.68 wt%. These results identify $LiRhH_3$ as a stable, ductile hydride and provide a basis for designing Rh-based perovskite hydrides for hydrogen storage and related energy applications.

* Corresponding author: tehreem.tariq@studenti.unipd.it (Tariq T.)
© 2026. All rights reserved.

1. Introduction

Rapid population growth and industrial expansion have greatly increased world energy consumption, which is still met mainly by fossil fuels [1]. These resources are finite, and their combustion releases greenhouse gases such as CO_2 that drive global warming; the use of low-efficiency, carbon-rich fuels alone has raised CO_2 emissions by almost 35%. The U.S. Energy Information Administration projects that world energy demand will rise by about 25% by 2040 [2]. To meet this demand, low-carbon sources such as solar, wind, hydrogen and nuclear energy are being developed, together with bioenergy routes that convert biomass and wastes into biogas and biomethane [3–5], bioethanol [6–8] and syngas [9].

Among these options, hydrogen is particularly attractive. It is non-toxic, has the highest energy content per unit mass of any common fuel and produces only water when oxidized, so it can serve as a clean energy carrier for homes, industry and transport. It can also be produced renewably, for example from lignocellulosic residues by dark fermentation [10, 11]. The main barriers to a hydrogen economy, however, are storage and transport [12, 13]. Research over the last decade has therefore focused on materials that store hydrogen at high gravimetric density near ambient pressure and temperature [14, 15]. Compressed-gas and liquid storage do not provide safe, low-cost, long-term storage [16], and high-pressure vessels made of high-strength steels also suffer from hydrogen embrittlement [17]. Solid-state storage is safer and more practical, and metal hydrides in particular combine good safety, easy handling and high hydrogen storage density [18–21].

Ternary perovskite hydrides ABH_3, in which A is an alkali or alkaline-earth metal (group IA or IIA) and B is a transition metal, are especially promising because they combine high storage capacity, good safety and reversible hydrogen uptake through chemical reactions at metal–hydrogen interfaces. First-principles calculations have become the main tool for screening these compounds. Xu et al. showed that XVH_3 (X = Na, K, Rb, Cs), $XAlH_3$ (X = Na, K) and $XTiH_3$ (X = K, Rb, Cs) are stable and suitable for hydrogen storage [22–24], Siddique et al. confirmed the structural, mechanical and dynamical stability of $LiAH_3$ (A = Sc, Ti, V) [25], and similar calculations have clarified hydrogen-diffusion kinetics in Mg–B–H phases [26] and the storage behavior of $LiMgF_3$ [19]. Rhodium is of particular interest because supported Rh and Rh-based alloy nanocatalysts are highly active for hydrogen release from chemical hydrogen storage materials [27]. Despite this, the physical properties of Rh-based perovskite hydrides remain largely unexplored.

In this work, the structural, electronic, mechanical, optical and hydrogen storage properties of the rhodium-based perovskite hydride $LiRhH_3$ were investigated by DFT using ultrasoft pseudopotentials, a plane-wave basis and the GGA–PBE functional [28]. The aims were to (i) confirm the structural and mechanical stability of cubic $LiRhH_3$, (ii) clarify its electronic nature and bonding, (iii) evaluate its optical response and (iv) estimate its theoretical hydrogen storage capacity, so as to guide experimental work on Rh-based hydrides for clean energy storage.

2. Computational methodology

The geometric structure was optimized and pertinent properties calculated using the Cambridge Serial Total Energy Package (CASTEP) technique [17, 29]. The first-principles method used in this research, based on DFT, ascertained the physical characteristics of these molecules. All the calculations performed in this work employed ultrasoft pseudopotentials. The GGA as proposed by Perdew, Burke, and Ernzerhof, was used to describe the electron-ion interactions that are based on the functional exchange-correlation. The electronic wave functions and charge densities of crystalline substances were calculated using the BFGS energy minimization technique [30]. A cutoff energy of 600 eV and Monkhorst-Pack k-point grid is used in the first Brillouin zone with a grid of $8 \times 8 \times 8$ for the material investigated. The conjugate gradient method was then employed to relax the lattice parameters, cell volume, and the positions of ions in the system to determine the energy properties of the system. Convergence energy was 2×10^{-1} eV/atom and Hellmann-Feynman forces were reduced to 0.05 eV/Å [23]. The elemental electronic configurations of the atoms investigated are: Li: $1s^2\ 2s^2$, Rhodium (Rh): $1s^2\ 2s^2\ 2p^6\ 3s^2\ 3p^6\ 4s^2\ 3d^{10}\ 4p^6\ 4d^8\ 5s^1$, and Hydrogen (H): $1s^1$. The maximum stress in all calculations was kept at 0.1 GPa. The elastic properties of the studied compounds were calculated using Voigt-Reuss-Hill (V-R-H) approximations, using the obtained elastic constants and optimized structures, U. Azhar et al. International Journal of Hydrogen Energy [24]. The electronic and optical characteristics were also studied after the optimization of geometry using the same mesh of k-points.

3. Results and discussions

3.1. Structural stability and geometry optimization

The optimized $LiRhH_3$ adopts the cubic ABH_3 perovskite structure (Fig. 1a), with Li on the 12-coordinate A site and Rh on the octahedral B site. Corner-sharing RhH_6 octahedra form a three-dimensional, tilt-free framework, and Li occupies the cuboctahedral cavities between them. Whether an ABX_3 composition adopts the cubic perovskite structure is commonly judged with tolerance-factor criteria [31]; the absence of octahedral tilting after full relaxation indicates that the Li/Rh size ratio is compatible with the ideal cubic arrangement. The simulated powder XRD pattern (Fig. 1b) shows strong (100), (110) and (111) reflections whose positions obey Bragg's law and give a single lattice parameter for all peaks [32]. The sharp, narrow reflections and the absence of superstructure or impurity peaks confirm a well-ordered cubic perovskite. The diffraction intensities are dominated by the Rh sublattice, because hydrogen scatters X-rays only weakly; the hydrogen positions are therefore fixed mainly by the optimized Rh–H geometry.

The electronic structure is shown in Fig. 2. Several bands cross the Fermi level (0 eV), most clearly along the R–M–Γ and Γ–R directions, and the total DOS remains finite but low at the Fermi energy. $LiRhH_3$ is therefore metallic rather than a band-gap semiconductor. The occupied states between about −12 and −4 eV arise mainly from Rh d–H 1s bonding states, with a dominant Rh d peak near −6 eV. The states above the Fermi level have mainly s and p character with only a small d contribution. Li contributes very little near the Fermi level and acts essentially as an electron-donating cation. The flat bands between about −5 and −7 eV correspond to strongly localized Rh d states, whereas the dispersive bands crossing the Fermi level carry the metallic conduction. The RhH_6 network therefore controls both charge transport and the optical response.

The XAS spectrum (Fig. 3a) shows a sharp absorption edge followed by several near-edge resonances, which correspond to transitions into unoccupied Rh d–H 1s antibonding states [33]. The emission spectrum reflects the occupied Rh d–H 1s bonding states. The electron-density map (Fig. 3b) shows little charge around Li and strong accumulation around Rh and along the Rh–H bonds. This indicates charge transfer from Li to the RhH_6 octahedra, with partly covalent Rh–H bonding inside an essentially ionic framework of Li^+ cations and $(RhH_3)^-$ units.

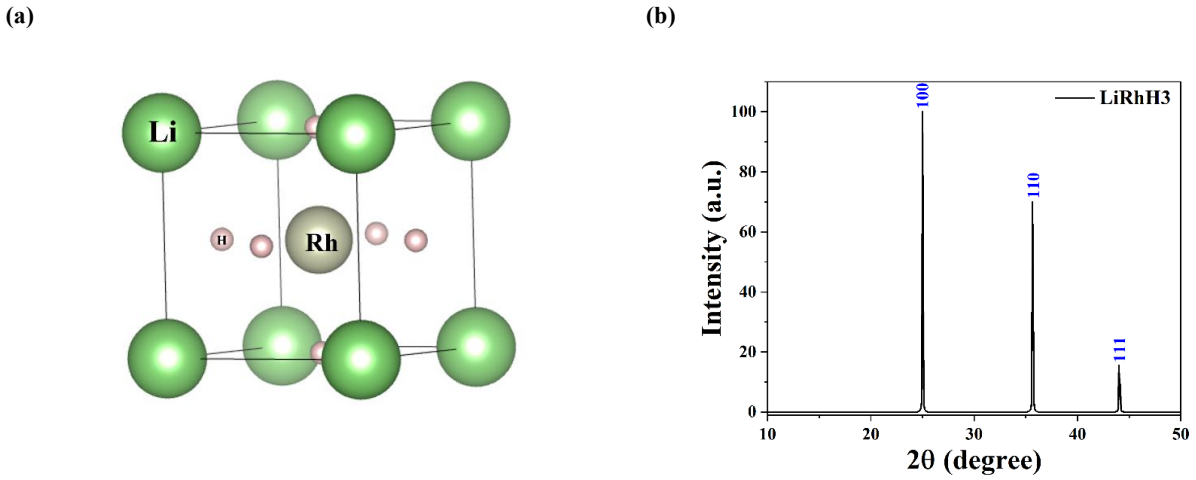


Fig. 1 (a) Optimized cubic crystal of LiRhH3 (b) X-ray diffraction (XRD) spectra.

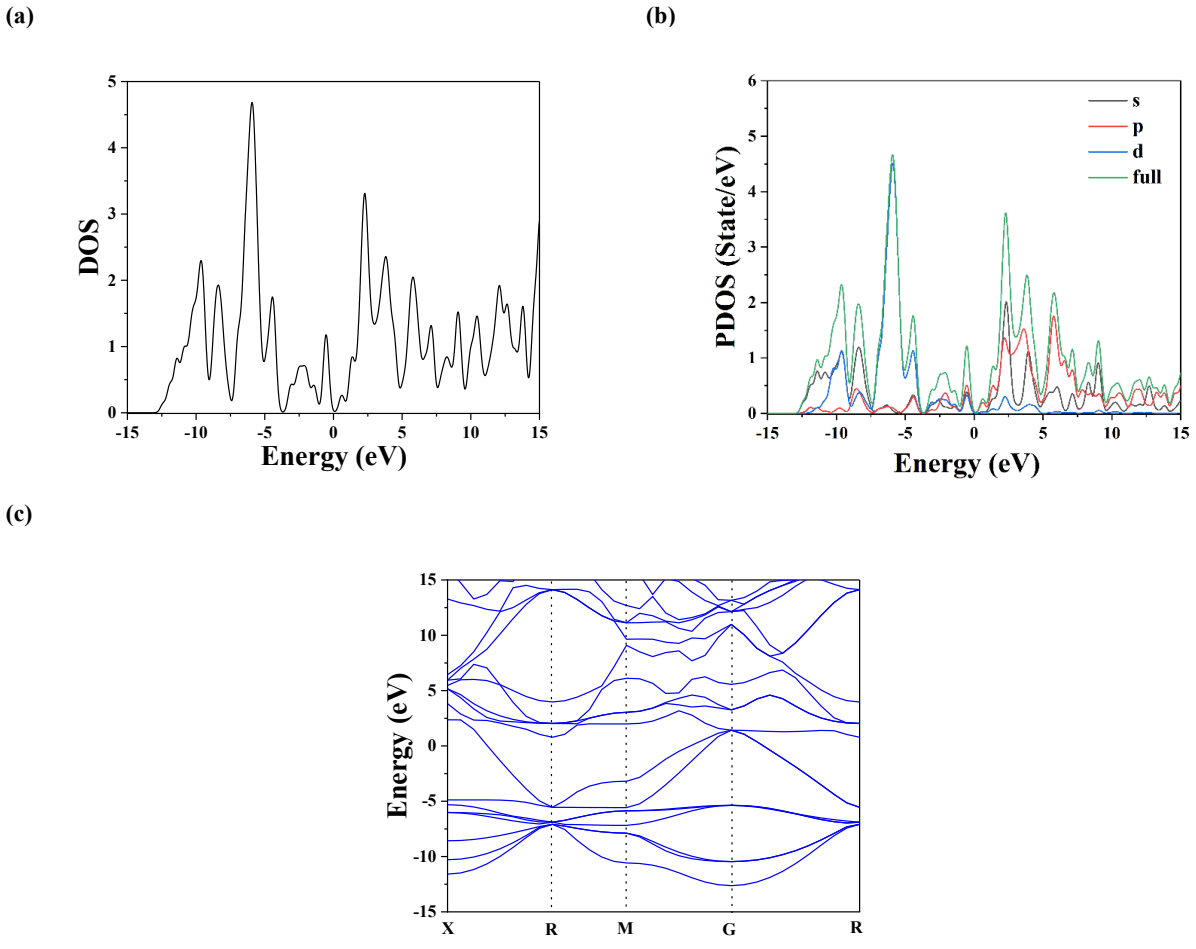


Fig. 2 (a) total density of states (b) partial density of states (PDOS), and (c) electronic band structure of LiRhH3

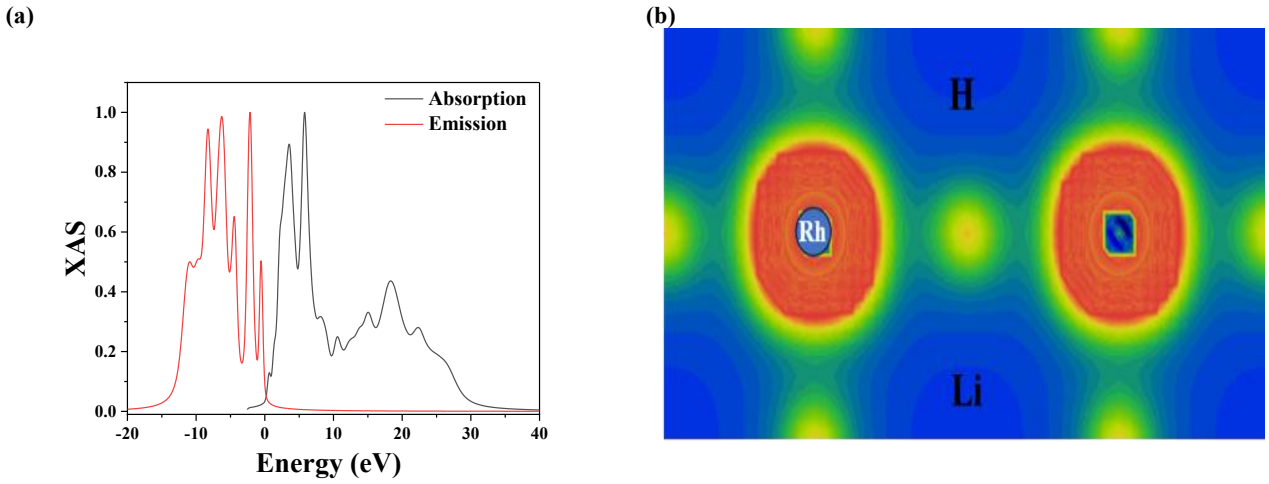


Fig. 3 (a) XAS absorbance and emission spectra (b) Electron-density distribution.

3.2. Mechanical properties

The elastic properties of $LiRhH_3$ determine its bonding strength, anisotropy and structural stability, and therefore its ability to withstand the repeated lattice strain of hydrogen absorption and desorption cycles [34]. During cycling, a hydride lattice expands and contracts by several percent, and materials that are too brittle tend to crack and decrepitate into fine powder, which degrades heat transfer and capacity over time. A reliable picture of the elastic response is therefore as important for a storage material as its hydrogen content.

For a cubic crystal, the elastic response is fully described by three independent constants. C_{11} measures the resistance to linear compression along the crystallographic axes, C_{12} couples a strain along one axis to the stress along a perpendicular axis, and C_{44} measures the resistance to shear on the {100} planes. The mechanical parameters discussed below were obtained from these constants using Eqs. (1)–(5). For a cubic crystal, the Born mechanical stability criteria are [35]:

$$C_{11} > 0, C_{44} > 0, C_{11} - C_{12} > 0, \text{requires.} \quad (1)$$

The computed elastic constants satisfy all of these criteria, so $LiRhH_3$ is mechanically stable in the cubic structure and no elastic instability is expected under small deformations. The Cauchy pressure, defined as $C_{12} - C_{44}$, gives further information on the bonding. A positive Cauchy pressure is characteristic of non-directional metallic or ionic bonding and is usually associated with ductile behavior, whereas a negative value indicates directional, covalent bonding and brittleness. The positive Cauchy pressure of $LiRhH_3$ therefore points to ductile behavior [35], in line with its metallic band structure (Fig. 2). The polycrystalline bulk modulus B, shear modulus G, Young's modulus E and Poisson's ratio ν were obtained with the Voigt–Reuss–Hill approximation, which averages the upper (Voigt) and lower (Reuss) bounds:

$$B = \frac{1}{3}(2C_{12} + C_{11}), G = \frac{G_R + G_V}{2}, \quad (2)$$

$$G_V = \frac{1}{3}(3C_{44} + C_{11} - C_{12}), G_R = \frac{5C_{44}(C_{11} - C_{12})}{4C_{44} + 3(C_{11} - C_{12})}, \quad (3)$$

$$E = \frac{9BG}{3B+G}, \nu = \frac{3B-2G}{3(3B+G)}. \quad (4)$$

The anisotropy factor is:

$$A = \frac{2C_{44}}{C_{11} - C_{12}}. \quad (5)$$

A large bulk modulus indicates strong resistance to volume change, whereas the shear modulus measures resistance to shape change and is more closely related to hardness. The calculated bulk modulus of $LiRhH_3$ is 91.015 GPa, so the lattice resists hydrostatic compression well. This is useful for a storage material, because a stiff framework is better able to keep its structural integrity while hydrogen is absorbed and released.

The ductility of $LiRhH_3$ was assessed with Pugh's ratio (B/G) and Poisson's ratio. Pugh's ratio exceeds the critical value of 1.75 and Poisson's ratio exceeds 0.25, and both criteria classify $LiRhH_3$ as ductile. A ductile hydride can accommodate the strain of repeated hydrogen cycling by plastic deformation rather than fracture, which reduces decrepitation and helps maintain capacity over many cycles. Poisson's ratio also reflects the type of bonding: values of about 0.1 are typical of covalent materials, whereas values near 0.25 or above are typical of ionic and metallic materials. The value obtained for $LiRhH_3$ is consistent with predominantly ionic bonding between Li^+ and the RhH_6 framework, in agreement with the charge transfer seen in the electron-density map (Fig. 3b), combined with metallic conduction within the Rh–H network.

Elastic anisotropy influences the formation of microcracks, the propagation of dislocations and the response of a material to directional stress. The directional dependence of Young's modulus, shear modulus, Poisson's ratio and linear compressibility is shown as 2D projections and 3D surfaces in Fig. 4 [36]. For an elastically isotropic solid, each of these surfaces would be a perfect sphere and

each 2D projection a circle, and the anisotropy factor A in Eq. (5) would equal 1.

The Young's modulus, shear modulus and Poisson's ratio surfaces of $LiRhH_3$ deviate clearly from spherical shape, so the stiffness and the lateral response of the crystal depend on the loading direction. This anisotropy means that, under the non-uniform stresses that develop during hydrogen uptake, some crystallographic directions will deform more easily than others, and grain boundaries between differently oriented crystallites may act as sites of stress concentration. In contrast, the linear compressibility is almost spherical, as required by cubic symmetry, so a hydrostatic pressure compresses the lattice uniformly in all directions. Overall, $LiRhH_3$ is mechanically stable, ductile, predominantly ionic and moderately anisotropic, a combination that is favorable for repeated hydrogen cycling.

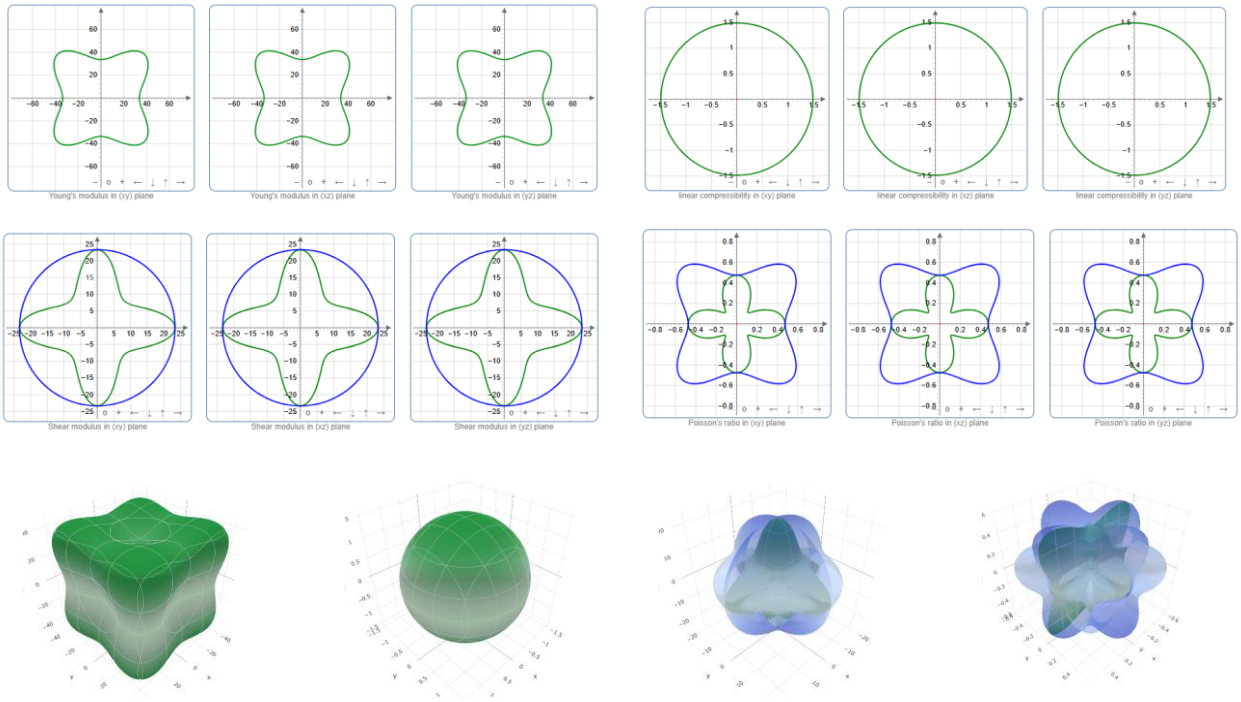


Fig. 4 2D and 3D Directional dependent elastic constants with Young's Modulus, Linear Compressibility, Shear Modulus, and Poisson's Ratio for $LiRhH_3$ perovskite hydrides.

3.3. Optical properties

Optical properties describe how a material interacts with electromagnetic radiation and are important for photocatalysis, solar energy conversion, hydrogen-related technologies and optoelectronics [37]. All of the optical quantities discussed here are derived from the complex dielectric function $\varepsilon(\omega) = \varepsilon_1(\omega) + i\varepsilon_2(\omega)$. The imaginary part $\varepsilon_2(\omega)$ is calculated from the momentum matrix elements between occupied and unoccupied states and describes the absorption of photons, while the real part $\varepsilon_1(\omega)$ is obtained from $\varepsilon_2(\omega)$ through the Kramers–Kronig relation and describes the polarization and dispersion of the material. The absorption coefficient, reflectivity, energy-loss function $-\mathrm{Im}[1/\varepsilon(\omega)]$, optical conductivity and refractive index then follow from ε_1 and ε_2, as given in Eqs. (6)–(8). Because the intraband (Drude) contribution of free carriers is usually not included in such calculations, the low-energy part of the spectra of a metallic compound such as $LiRhH_3$ should be interpreted with care.

$$\varepsilon(\omega) = \varepsilon_1(\omega) + i\varepsilon_2(\omega). \quad (6)$$

The refractive index and reflectivity are given by:

$$n(\omega) = \left[\frac{\varepsilon_1(\omega)}{2} + \left(\frac{\varepsilon_1^2(\omega)+\varepsilon_2^2(\omega)}{4}\right)^{1/2}\right]^{1/2}, \quad (7)$$

$$R(\omega) = \frac{(n+ik)-1}{(n+ik)+1}. \quad (8)$$

The optical spectra of $LiRhH_3$ are shown in Fig. 5 over a photon energy range of 0–50 eV. Absorption (Fig. 5a) is strongest in the ultraviolet, with a maximum near 291 nm (about 4.3 eV), and decreases steadily through the visible range, becoming very weak above about 700 nm. $LiRhH_3$ therefore interacts mainly with ultraviolet light and is largely transparent in the near-infrared. The absorption maximum lies close to the first strong peak of ε_2 at 4.6 eV, which confirms that it arises from interband transitions.

The reflectivity (Fig. 5b) remains below about 0.35 over the whole range. It shows major peaks at about 3.2, 7.2, 10.0, 12.7, 14.6, 20.2 and 22.1 eV and falls sharply above about 30 eV, where the material becomes largely transparent. The energy-loss function (Fig. 5c) describes the energy lost by a fast electron passing through the material and reaches its maximum of 3.04 at 23.76 eV. This peak corresponds to the bulk plasma frequency, at which collective oscillations of the valence electrons are excited.

It lies just above the last reflectivity maximum at 22.1 eV and coincides with the steep fall in reflectivity, as expected for a plasma edge.

The imaginary part of the dielectric function (Fig. 5d), which reflects interband absorption, shows strong peaks at 4.6, 6.3, 8.9 and 13.6 eV, with weaker features at 41.7 and 49.4 eV. The low-energy peaks correspond to transitions from the occupied Rh d–H 1s states into empty states above the Fermi level (Fig. 2), while the weak high-energy features arise from deeper-lying states. The real part peaks at 2.6 eV, dips at 3.9 eV and becomes slightly negative between about 12 and 17 eV, where the material reflects rather than transmits light. The static value $\varepsilon_1(0)$ is about 7.

The refractive index and extinction coefficient (Fig. 5e) show strong features at low energy and many peaks up to about 12 eV, followed by weak structure above 38 eV. The static refractive index n(0) is about 2.6, which is consistent with the static dielectric constant because $n(0)^2 \approx \varepsilon_1(0)$. The refractive index rises to a maximum of about 3.3 near 2.5 eV and then decreases at higher energies, while the extinction coefficient follows the absorption. The optical conductivity (Fig. 5f) forms a main band between about 14 and 16 eV with several weaker peaks at higher energy, and its imaginary part extends as a broad tail to 50 eV. These features mirror the interband structure of ε_2 and show that photon absorption creates mobile charge carriers over a wide energy range.

Taken together, the optical response of $LiRhH_3$ is dominated by interband transitions involving the Rh d–H 1s states. The strong ultraviolet absorption, moderate refractive index and low reflectivity in the visible range suggest that $LiRhH_3$ may also be useful in UV-shielding coatings and UV optoelectronic devices. Moreover, because hydrogen uptake and release change the electronic structure of a hydride, optical measurements in the UV region could serve as a simple, non-destructive way to monitor the hydrogenation state of $LiRhH_3$-based materials.

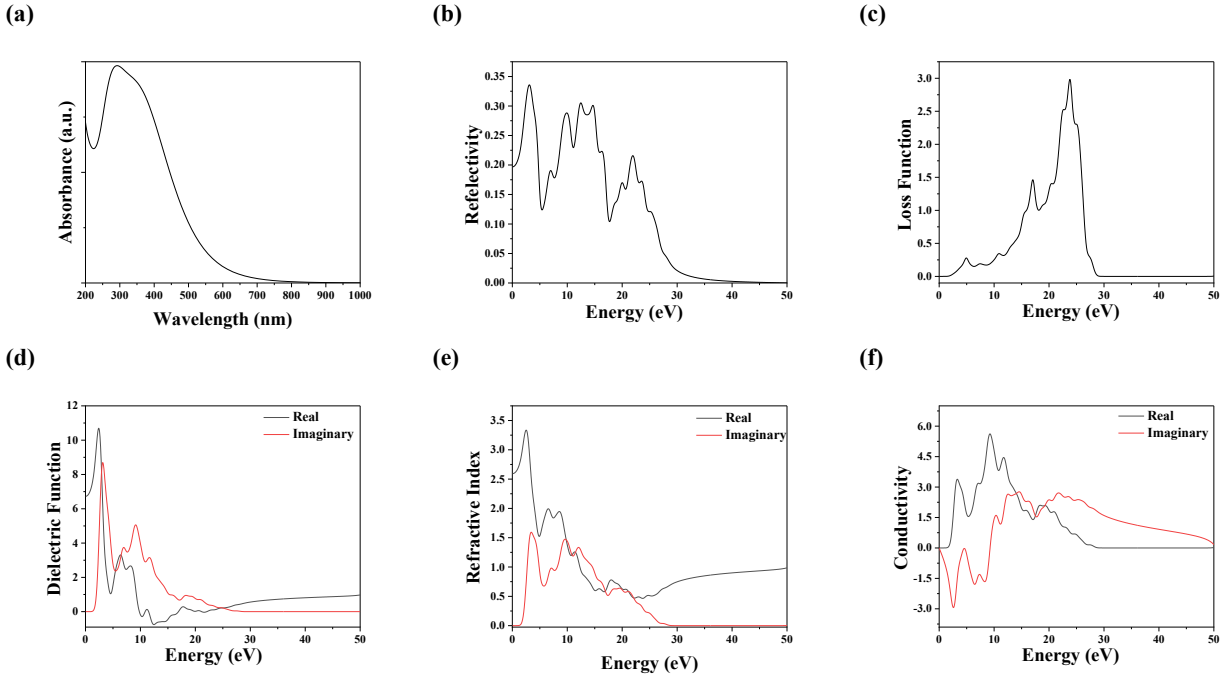


Fig. 5 Optical properties of the composites, (a) Absorption, (b) reflectivity. (c) Loss function, (d) variation in the imaginary and real parts of the dielectric function, (e) refractive Index-imaginary, and (f) conductivity.

3.4. Gravimetric hydrogen storage capacity

The gravimetric hydrogen storage capacity is the most widely used figure of merit for a hydrogen storage material. It was estimated as $C = (n \cdot A(H)/M) \times 100$ wt%, where n is the number of hydrogen atoms per formula unit, A(H) = 1.008 g mol^{-1} is the atomic mass of hydrogen and M is the molar mass of the hydride [23, 24]. For $LiRhH_3$ (n = 3, M = 112.87 g mol^{-1}), this gives C ≈ 2.68 wt%, which corresponds to a hydrogen-to-metal ratio (H/M) of 1.5.

To place this value in context, the same expression was applied to other perovskite hydrides studied by first-principles methods. It gives 5.51, 5.23 and 4.97 wt% for $LiScH_3$, $LiTiH_3$ and $LiVH_3$ [25], 5.71 and 4.38 wt% for $NaAlH_3$ and $KAlH_3$ [23], 3.93 wt% for $NaVH_3$ [22] and 3.36 wt% for $KTiH_3$ [24]. $LiRhH_3$ thus has a lower gravimetric capacity than these compounds and than light-metal hydrides such as MgH_2 (7.6 wt%) [21]. The reason is the large atomic mass of Rh (102.91 g mol^{-1}), which accounts for about 91% of the molar mass of the compound, while the number of hydrogen atoms per formula unit is the same in all ABH_3 hydrides.

Gravimetric capacity alone does not decide whether a hydride is useful, however. Mechanical stability, ductility, reversibility, kinetics and the thermodynamics of hydrogen release are equally important. $LiRhH_3$ combines

mechanical stability with ductile, predominantly ionic behavior, which favors durability over many absorption–desorption cycles, and its metallic character may support fast electron transfer during hydrogen uptake and release. It is therefore most relevant for applications where stability and cycle life matter more than weight, such as stationary storage. Two routes could raise its capacity: partial substitution of Rh by lighter transition metals such as Ti or V, and replacement of Li-site or Rh-site atoms to tune the hydrogen binding energy. Future work should also calculate the formation enthalpy and hydrogen desorption temperature of $LiRhH_3$, as well as its volumetric capacity, to complete the assessment of its storage performance.

4. Conclusion

In this, we investigated the physical characteristics of $LiRhH_3$ perovskite hydrides based on rhodium. Rhodium improves the mechanical, electrical, and thermodynamic properties of the perovskite structure, increasing its durability and stability. The electronic band structures showed a zero band gap, indicating metallic behavior, and geometry optimization validated structural stability. Based on Pugh's ratio and Poisson's ratio, the material was demonstrated to be ionic, ductile, and anisotropic after elastic constants were computed to confirm mechanical stability. These results offer a strong basis for future investigation, moving hydride perovskites from theoretical study to real-world uses.

References

[1] Zou, C., Zhao, Q., Zhang, G., & Xiong, B. (2016). Energy revolution: From a fossil energy era to a new energy era. *Natural Gas Industry B, 3*(1), 1–11.

[2] Conti, J., Holtberg, P., Diefenderfer, J., LaRose, A., Turnure, J. T., & Westfall, L. (2016). *International energy outlook 2016 with projections to 2040*. U.S. Energy Information Administration.

[3] Ramaraj, R., Junluthin, P., Dussadee, N., & Unpaprom, Y. (2025). Potential evaluation of biogas production through the exploitation of naturally growing freshwater macroalgae *Spirogyra varians*. *Environment, Development and Sustainability, 27*(9), 22551–22562. https://doi.org/10.1007/s10668-021-02051-2

[4] Sabarikirishwaran, P., Shen, M. Y., Ramaraj, R., Unpaprom, Y., Wu, H. C., & Chu, C. Y. (2023). Feasibility and optimizing assessments on biogas and biomethane productions from *E. coli* fermenter effluent. *Biomass and Bioenergy, 173*, 106783. https://doi.org/10.1016/j.biombioe.2023.106783

[5] Ramaraj, R., Nong, H. T. T., & Unpaprom, Y. (2025). Enhancing biomethane through co-digestion of water primrose and cow dung insights into effective biogas purification techniques. *Fuel, 399*, 135654. https://doi.org/10.1016/j.fuel.2025.135654

[6] Trejo, M., Bhuyar, P., Velu, G., Pérez, E. Z., Unpaprom, Y., Trail, A., & Ramaraj, R. (2022). The effect of various pretreatments conditions on the distribution of fermentable sugar from dried elephant ear plant. *Fuel, 324*, 124624. https://doi.org/10.1016/j.fuel.2022.124624

[7] Bautista, K., Unpaprom, Y., Junluthin, P., & Ramaraj, R. (2025). Ethanol production from corn stalk juice by *Saccharomyces cerevisiae* immobilized yeast using a green method. *Biomass Conversion and Biorefinery, 15*(2), 1893–1900. https://doi.org/10.1007/s13399-021-02261-8

[8] Ramaraj, R., Unpaprom, Y., Ramaraj, R., & Dussadee, N. (2026). An integrated multi-criteria decision framework for cascading low-grade longan into bioethanol and methane-rich biogas. *Journal of Intelligent Decision Making and Information Science, 3*(8s), 1333–1359. https://doi.org/10.59543/jidmis.v3.2193

[9] Dussadee, N., Ramaraj, R., Homdoung, N., & Sasujit, K. (2026). Invasive weed, intelligent solution: A multi-criteria framework for water-hyacinth gasification, GIS resource assessment, and techno-economic deployment. *Journal of Intelligent Decision Making and Information Science, 3*(9s), 2817–2841. https://doi.org/10.17762/jidmis.v3.2569

[10] Chatnarin, S., Unpaprom, Y., Ramaraj, R., & Chu, C. Y. (2025). Enhanced bio-hydrogen production from furniture industry bamboo waste: Optimization of pretreatment and co-fermentation processes. *Fuel, 401*, 135933. https://doi.org/10.1016/j.fuel.2025.135933

[11] Panyakularak, S., Pomdaeng, P., Unpaprom, Y., Ramaraj, R., & Chu, C. Y. (2026). Effects of different dewaxing methods combined with acid pretreatment on biohydrogen production from cinnamon leaves. *Biomass and Bioenergy, 208*, 108866. https://doi.org/10.1016/j.biombioe.2025.108866

[12] Gür, T. M. (2018). Review of electrical energy storage technologies, materials and systems: Challenges and prospects for large-scale grid storage. *Energy & Environmental Science, 11*(10), 2696–2767.

[13] Wieliczko, M., & Stetson, N. (2020). Hydrogen technologies for energy storage: A perspective. *MRS Energy & Sustainability, 7*, E41.

[14] Züttel, A. (2004). Hydrogen storage methods. *Naturwissenschaften, 91*(4), 157–172.

[15] Schlapbach, L., & Züttel, A. (2001). Hydrogen-storage materials for mobile applications. *Nature, 414*(6861), 353–358. https://doi.org/10.1038/35104634

[16] Aziz, M. (2021). Liquid hydrogen: A review on liquefaction, storage, transportation, and safety. *Energies, 14*(18), 5917.

[17] Meda, U. S., Bhat, N., Pandey, A., Subramanya, K., & Raj, M. L. A. (2023). Challenges associated with hydrogen storage systems due to the hydrogen embrittlement of high strength steels. *International Journal of Hydrogen Energy, 48*(47), 17894–17913.

[18] Zheng, J., et al. (2021). Current research trends and perspectives on solid-state nanomaterials in hydrogen storage. *Research*.

[19] Mubashir, M., Ali, M., Bibi, Z., Younis, M., & Muzamil, M. (2024). Efficient hydrogen storage in $LiMgF_3$: A first principle study. *International Journal of Hydrogen Energy, 50*, 774–786.

[20] Rusman, N., & Dahari, M. (2016). A review on the current progress of metal hydrides material for solid-state hydrogen storage applications. *International Journal of Hydrogen Energy, 41*(28), 12108–12126.

[21] Sakintuna, B., Lamari-Darkrim, F., & Hirscher, M. (2007). Metal hydride materials for solid hydrogen storage: A review. *International Journal of Hydrogen Energy, 32*(9), 1121–1140. https://doi.org/10.1016/j.ijhydene.2006.11.022

[22] Xu, N., et al. (2023). First-principles investigations for the hydrogen storage properties of XVH_3 (X = Na, K, Rb, Cs) perovskite type hydrides. *Journal of Materials Research and Technology, 26*, 4825–4834.

[23] Xu, N., et al. (2024). First-principles study on hydrogen storage properties of the new hydride perovskite $XAlH_3$ (X = Na, K). *International Journal of Hydrogen Energy, 60*, 434–440.

[24] Xu, N., Chen, Y., Chen, S., Li, S., & Zhang, W. (2024). First-principles investigation for the hydrogen storage properties of

$XTiH_3$ (X = K, Rb, Cs) perovskite type hydrides. *International Journal of Hydrogen Energy, 50*, 114–122.

[25] Siddique, A., et al. (2023). Structural, electronic, mechanical and dynamical stability properties of $LiAH_3$ (A = Sc, Ti & V) perovskite-type hydrides: A first principle study. *Chemical Physics, 568*, 111851.

[26] Sukmas, W., et al. (2023). First-principles calculations on superconductivity and H-diffusion kinetics in Mg–B–H phases under pressures. *International Journal of Hydrogen Energy, 48*(10), 4006–4015.

[27] Sun, Q., Wang, N., Xu, Q., & Yu, J. (2020). Nanopore-supported metal nanocatalysts for efficient hydrogen generation from liquid-phase chemical hydrogen storage materials. *Advanced Materials, 32*(44), 2001818.

[28] Perdew, J. P., Burke, K., & Ernzerhof, M. (1996). Generalized gradient approximation made simple. *Physical Review Letters, 77*(18), 3865–3868. https://doi.org/10.1103/PhysRevLett.77.3865

[29] Clark, S. J., Segall, M. D., Pickard, C. J., Hasnip, P. J., Probert, M. I. J., Refson, K., & Payne, M. C. (2005). First principles methods using CASTEP. *Zeitschrift für Kristallographie, 220*(5–6), 567–570. https://doi.org/10.1524/zkri.220.5.567.65075

[30] Pfrommer, B. G., Côté, M., Louie, S. G., & Cohen, M. L. (1997). Relaxation of crystals with the quasi-Newton method. *Journal of Computational Physics, 131*(1), 233–240. https://doi.org/10.1006/jcph.1996.5612

[31] Bartel, C. J., et al. (2019). New tolerance factor to predict the stability of perovskite oxides and halides. *Science Advances, 5*(2), eaav0693.

[32] Kim, D., & Heller, E. J. (2022). Bragg scattering from a random potential. *Physical Review Letters, 128*(20), 200402.

[33] Rothenbach, N., et al. (2021). Effect of lattice excitations on transient near-edge x-ray absorption spectroscopy. *Physical Review B, 104*(14), 144302.

[34] Saini, R. S., Mosaddad, S. A., & Heboyan, A. (2023). Application of density functional theory for evaluating the mechanical properties and structural stability of dental implant materials. *BMC Oral Health, 23*(1), 958.

[35] Gao, J., Liu, Q.-J., & Tang, B. (2023). Elastic stability criteria of seven crystal systems and their application under pressure: Taking carbon as an example. *Journal of Applied Physics, 133*(13).

[36] Leheny, S., et al. (2021). Directional dependence of the mechanical properties of aged paper. *Mechanics of Materials, 162*, 104036.

[37] Hassaan, M. A., El-Nemr, M. A., Elkatory, M. R., Ragab, S., Niculescu, V.-C., & El Nemr, A. (2023). Principles of photocatalysts and their different applications: A review. *Topics in Current Chemistry, 381*(6), 31.